

The Boundary Element Method in Fluid Mechanics: Application to Bubble Growth

A. López-Villa, Luis S. Zamudio and A. Medina

Abstract The origin of the numerical implementation of boundary integral equations can be traced from fifty years earlier, when the electronic computers had become available. The full emergence of the numerical technique known as the boundary element method occurred in the late 1970s. In implementing the method, only the boundary of the solution domain has to be discretized into elements. In the case of a two-dimensional problem, this is really easy to do: put closely packed points on the boundary (a curve) and join up two consecutive neighboring points to form straight line elements. In this chapter we present one of the applications of this method, namely, the growth and detachment of bubbles generated by the continuous injection of gas into a quiescent liquid and the effect of partial confinement on the shape and volume of bubbles generated by injection of a constant flow rate of gas. In the problem of bubble generation, the contours are the surfaces of the bubbles and the solid surfaces of the reservoir, which are all surfaces of revolution. The unknowns involved in the formulation of the boundary element are fluid particle velocities that define surfaces of the bubbles and the stresses on the vessel wall. First, we neglect viscous effects and assume the flow to be irrotational so that a velocity potential exists. In second case we solve the Stokes equations for the liquid and the evolution equation for the surface of a bubble. Experiments with two different liquids show that cylindrical and conical walls and cylinder walls with periodic concentric corrugations with a gas injected through an orifice at the bottom of the liquid may strongly affect the shape and volume of the bubbles, and can be used to control the size of the generated bubbles without changing the flow rate of gas.

A. López-Villa (✉) · A. Medina

ESIME Azcapotzalco, Instituto Politécnico Nacional, Av. de las Granjas
No. 682, Col. Sta. Catarina, 02550 México, D.F., México
e-mail: abelvilla77@hotmail.com

Luis S. Zamudio

Programa de Ingeniería Molecular, Grupo de Química Aplicada a la Industria Petrolera, Instituto Mexicano del Petróleo, eje Central Lázaro Cárdenas
No. 152, col, San Bartolo Atepehuacan, 07730 México, D.F., México

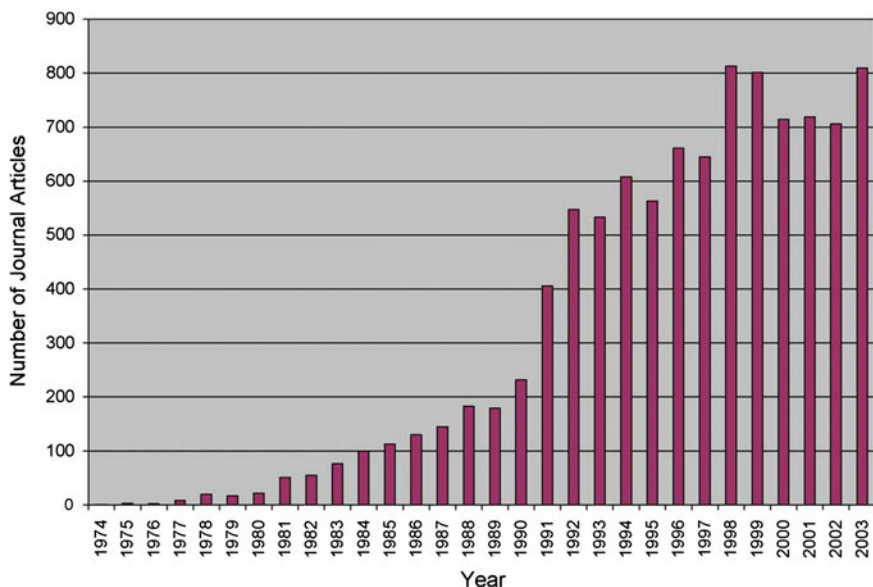


Fig. 1 Number of journal articles published by the year on the subject of BEM, based on the Web of Science search. Refer to Appendix for the search criteria (Search date: May 3, 2004)

1 Introduction

Mathematicians from the eighteenth to twentieth centuries, whose contributions were the key to the theoretical development, are honored with short biographies. The origin of the numerical implementation of boundary integral equations can be traced back to the 1960s, when the electronic computers had become available.

The full emergence of the numerical technique known as the boundary element method occurred in the late 1970s. This article reviews the early history of the boundary element method up to the late 1970s.

After three decades of development, the boundary element method (BEM) has found a firm footing in the area of numerical methods for partial differential equations. Comparing to the more popular numerical methods, such as the Finite Element Method (FEM) and the Finite Difference Method (FDM), which can be classified as the domain methods, the BEM distinguish itself as a boundary method, meaning that the numerical discretization is conducted at reduced spatial dimension. For example, for problems in three spatial dimensions, the discretization is performed on the bounding surface only; and in two spatial dimensions, the discretization is on the boundary contour only. This reduced dimension leads to smaller linear systems, less computer memory requirements, and more efficient computation. This effect is most pronounced when the domain is unbounded. Unbounded domain needs to be truncated and approximated in domain methods. The BEM, on the other hand, automatically models the behavior at infinity without the need of deploying a mesh to approximate it. Figure 1 presents the histogram of the number of journal papers

published annually, containing BEM as a keyword (Alexander and Daisy 2005; Costabel Martin 1986).

Because a given set of boundary and initial conditions uniquely define the solution in the domain, the value of the function at any point in the interior can be expressed as a sole contribution of boundary values, what is achieved mathematically by the Green-Stokes-Gauss-divergence theorem, which is the foundation of the boundary elements method (BEM). With this method, first the full solution (function and derivatives) at the boundary points are computed by a kind of finite-element method where the base functions are the fundamental solutions of the PDE at the boundary nodes, then solving a set of algebraic equations at the nodes, and finally, if needed, the value at any internal point is directly computed by a quadrature (without interpolation).

The problem with the boundary element method is that the local integration in the boundary is more involved than in the standard FEM because there are singular points that require more elaborated computations. Other handicap is that the BEM only applies to regions of constant properties. The great advantage is that for bulky domains the number of nodes significantly decreases, particularly for infinite domains (what explains its massive use in external fluid mechanics and geomechanics). Incidentally, for infinite domains, besides the BEM, one may also resort to classical FEM with a truncated domain progressively enlarged, or matched to an asymptotic analytical expansion, or stretching the external elements with a log-transformation.

On the other hand, the growth and detachment of bubbles generated by the continuous injection of gas into a quiescent liquid has been very much studied in conditions where the viscosity of the liquid plays no important role (Davidson and Schuler 1960; Longuet-Higgins et al. 1991; Marmur and Rubin 1976; Clift et al. 1978; Corchero et al. 2006). Results of these studies are of interest in metallurgical and chemical industries among others, where liquids of low viscosity, such as liquid metals and aqueous solutions, need to be handled. Bubbles in these liquids can be used to modify the concentrations of different substances and promote chemical reactions between them, to clean liquids from impurities captured by adhesion or diffusion processes, and for many other purposes (López-Villa et al. 2011).

The generation and dynamics of bubbles in very viscous liquids is also of interest but has not been so much studied. Thus, while many aspects of the dynamics of bubbles in unbounded viscous liquids are well understood, the formation and detachment of bubbles in confined systems has received less attention. Bubbles in very viscous liquids are commonly found when dealing with polymers in their liquid phases, in the flows of lava, and in processes of oil extraction from production pipelines, among others. The latter example is a motivation of the present work, which sprang from interest in the so-called gas lift technique of enhanced oil recovery, where bubbles formed by injecting gas in oil extraction pipes help pumping the oil. Another motivation is the foam formation, where we study the problem of the film thickness that is formed between the free surface of a single bubble and the wall when the bubble reaches its critical size in the vertical circular tube with smooth or ribbed walls filled with a quiescent liquid of high viscosity. The foam formation is very important for enhanced oil recovery (EOR), where the foam is used for channeling oil and clogs the fractures to keep out gas, in fractured oil reservoirs. If gas mobility can be controlled,

oil displacement efficiency is improved (Kovscek et al. 1995). Foam is a promising general agent for controlling gas mobility in EOR processes (Hirasaki and Lawson 1985) and in other applications, such as aquifer storage of natural gas (Witherspoon et al. 1987) and compressed air.

Scaling laws show that the volume of the bubbles generated by injecting a high flow rate of gas into a very viscous liquid increases as the power $3/4$ of the flow rate and is independent of the diameter of the injection orifice. The simplest way to control the size of the bubbles in a given liquid is, therefore, to act on the flow rate of gas. This possibility, however, is limited in the application at hand, because the flow rate of gas to be injected in the confined space of an extraction pipe is often determined by other requirements of the gas lift technique. The limitation poses a problem to control the size of the bubbles and brings to the front elements of the generation process such as the viscous drag of the bubbles and the shear stress in the vicinity of the walls, which are disregarded in inviscid analyses but offer a clue to the solution of the size-control problem. In this chapter, we first neglect viscous effects and assume the flow to be irrotational so that a velocity potential exists; in second case we solve the Stokes equations for the liquid and the evolution equation for the surface of a bubble. The shape of the tube in the vicinity of the injection orifice, or the use of properly shaped injection nozzles, may cause substantial distortion of the growing and shape of the bubbles and modify their volume at detachment. In our analysis, a constant flow rate of gas is injected through a circular orifice at the horizontal base of a container filled with non-viscous and very viscous liquid, and the space where the bubbles grow can be partially confined by surrounding the orifice with a vertical cylindrical wall or an inverted vertical cone. The extent of the confinement can be gradually increased by decreasing the radius of the cylinder or the angle of the cone, which allows quantifying the effect of the wall on the evolution and size of the bubbles. This size is determined numerically and experimentally, and scaling laws that are extensions of well-known laws for unconfined liquids are proposed and validated.

To reach our goal the structure of the chapter is as follows. In the next section we formulate the problem in terms of dimensionless equations for the motion of the non-viscous liquid and the dimensionless boundary conditions for the evolution of the free surface. In Sect. 3 we formulate the problem in terms of dimensionless equations of motion of viscous fluids and the dimensionless boundary conditions for the evolution of the free surface. In Sect. 4 we briefly explain the BEM method. The main results of the numerical solution of this problem are given in Sect. 5, discussing the evolution of the free surface during the growth of the bubble at constant gas flow rate in conical and cylindrical containers. In Sect. 6 we compare some qualitative experiments to our numerical results. Finally, Sect. 7 summarizes the main findings and limitations of this work.

2 Equations for Bubbles in Non-Viscous Liquids

Generation of bubbles by injection of a gas into a liquid at rest is an important and much studied problem. Extensive research has been summarized in a variety of models that address the many facets of the problem with different levels of detail; see Clift et al. (1978), Rübiger and Vogelpohl (1986), Tsuge (1986) and Sadhal et al. (1997) for reviews. The conceptually simplest models are based on a balance of the forces acting on a bubble of assumed shape (see Davidson and Schuler (1960), among others). These models clearly show the existence of a regime of low gas flow rate in which the effect of the inertia of the liquid is negligible and the volume of the bubbles is a constant independent of the gas flow rate, and a regime of high gas flow rate in which the effect of the surface tension is negligible and the volume of the bubbles increases as the $6/5$ power of the gas flow rate and is independent of the size of the injection orifice.

The original models of Davidson and Schuler (1960) and Ramakrishna et al. (1968) which served to establish these results, have been extended to include a variety of effects such as the viscous drag of the bubbles, the flow left by the viscous wake of the preceding bubble, the momentum flux of the injected gas, and the different shapes and apparent masses of the bubble at different stages of its growth. Extensions also include a set of ad hoc criteria to account for the interference, collision and coalescence of bubbles (Zhang and Shoji 2001), which are observed to occur at high flow rates and eventually lead to non-periodic and chaotic regimes of bubble generation (Leighton et al. 1991). More sophisticated non-spherical models (Marmur and Rubin 1976) postulate equations of motion for each element of the bubble surface, whose shape changes continuously during the growth and detachment. These models rely on varying degrees of solutions for the potential flow of the liquid (Wraith and Kakutani 1974). Oguz and Prosperetti (1993) numerically computed this flow using a boundary element method and described in full detail the growth and detachment of a single bubble at the end of a tube in different cases of interest, finding good agreement with high speed video visualizations (see also Oguz and Zeng 1997).

This section focuses on time periodic bubbling regimes featuring coalescence of two or more bubbles in a strictly inviscid liquid. Though the bubble generation process ceases to be periodic when the flow rate is increased to sufficiently high values, these more complex regimes will not be discussed here. Instead, the purpose of the work is to examine to what extent coalescence at moderate gas flow rates can be described in the framework of potential flow theory. In this respect, the work is an extension of those of Oguz and Prosperetti (1993) and Oguz and Zeng (1997) to include bubble coalescence. The main result is that potential flow computations suffice to describe many aspects of coalescence, without resorting to any wake effect or other effects related to the viscosity of the liquid.

Attention will be restricted to the simplest case of injection of a constant flow rate of a gas through a single circular orifice at the bottom of an inviscid liquid at rest (see Fig. 2). The gas will be treated as incompressible, with a density negligibly small compared to the density of the liquid. The only parameters of the problem are

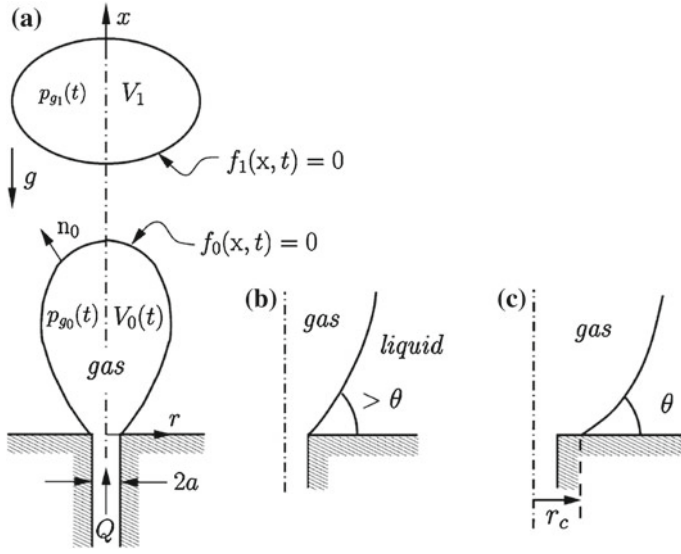


Fig. 2 Definition sketch (a), with details of the contact line attached to the edge of the orifice (b) and spreading on the horizontal bottom (c)

then the radius of the orifice, a , the density of the liquid, ρ , the liquid–gas surface tension, σ , the contact angle of the surface with the bottom, θ , the gas flow rate, Q (volume of gas injected per unit time), and the acceleration due to gravity, g . The dimensional parameters can be grouped into a Bond number and a Weber number:

$$B = \frac{\rho g a^2}{\sigma} \quad We = \frac{\rho Q^2}{\sigma a^3} \quad (1)$$

The flow induced in the liquid by the train of bubbles released from the orifice is irrotational if the viscosity of the liquid is neglected. The velocity potential, φ , such that $v = \nabla \varphi$, satisfies the Laplace equation

$$\nabla^2 \varphi = 0 \quad (2)$$

in the liquid, to be solved with the conditions

$$\frac{Df_i}{Dt} = 0, \quad (3)$$

$$\frac{D\varphi}{Dt} = \frac{1}{2} |\nabla \varphi|^2 - p_{gi} - Bx + \nabla \cdot n_i, \quad (4)$$

at the surfaces of the bubbles; and $\frac{\partial \varphi}{\partial x} = 0$ at the bottom ($x = 0$) and $\nabla \varphi \rightarrow 0$ at infinity. Here $f_i(x, t) = 0$ is the equation of the surface of the i -th bubble, with $i = 0$ denoting the bubble growing at the orifice and $i = 1, 2, \dots$ denoting the bubbles detached previously. These surfaces are to be found as part of the solution. Distances and times are non-dimensionalized with the radius of the orifice a and the capillary time $(\rho a^3 / \sigma)^{1/2}$. In Eq. (4) x is the dimensionless height above the bottom, $\frac{D}{Dt} = \frac{\partial}{\partial t} + \mathbf{v} \cdot \nabla$ is the material derivative at points of the bubble surfaces, $\mathbf{n}_i = \nabla f_i / |\nabla f_i|$, and p_{gi} is the gas pressure in the i -th bubble referred to the pressure of the liquid at the bottom far from the orifice and scaled with a factor a / σ . These pressures are functions of time which are determined by the conditions that the volume of the growing bubble ($i = 0$) increases at a constant rate equal to the volume of gas injected per unit time (Q), and the volumes of the detached bubbles ($i = 1, 2, \dots$) do not change with time.

An additional condition is needed at the contact line of the growing bubble with the solid. Here the contact line will be taken to coincide with the edge of the orifice when the angle of the liquid–gas surface with the horizontal is larger than the contact angle (i.e. when $-\mathbf{n}_{x0} < \cos \theta$, where \mathbf{n}_{x0} is the vertical component of the unit normal \mathbf{n}_0 to the attached bubble, see Fig. 2), and to spread away from the orifice with the liquid–gas surface making a constant contact angle with the solid ($-\mathbf{n}_{x0} = \cos \theta$) otherwise. The two possibilities are sketched in Figs. 2b and c. The contact angle θ is a third parameter of the problem, along with B and We defined in (1). Time periodic, axisymmetric solutions of the problem have been computed numerically using a standard boundary element method to solve the Laplace equation and a second order Runge–Kutta method to advance the material nodes at the surfaces of the bubbles and the velocity potential at them according to (3) and (4), with $p_{gi}(t)$ determined at each time step. The implementation follows that of Oguz and Prosperetti (1993).

The final volume of the bubbles is shown in Fig. 3 as a function of the dimensionless flow rate $We^{1/2}$ for two different values of the Bond number, $B = 0.1$ and $B = 1$, which correspond to orifices of radii $a = 0.85$ and 2.68 mm, respectively, in pure water. The contact angle was taken as $\theta = 45^\circ$ though results for other values of θ are qualitatively similar.

Numerical computations have been carried out of the axisymmetric, irrotational, time periodic flow induced in a quiescent strictly inviscid liquid by the growth, detachment and coalescence of bubbles (see Figs. 4 and 5) due to the injection of a constant gas flow rate through a horizontal submerged orifice. The results show that this simple potential flow formulation may qualitatively describe many aspects of the well-known transition from quasi-static generation of independent, constant volume bubbles at low Weber numbers to inertia and buoyancy controlled growth and interaction of bubbles at moderately high Weber numbers.

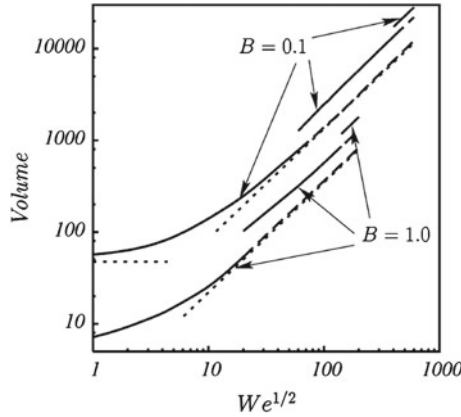


Fig. 3 Volume of the bubbles scaled with a^3 as a function of the dimensionless gas flow rate $We^{1/2}$ for $B = 0.1$ (upper set of curves) and $B = 1$ (lower set of curves). The solid curves of each set give the final volume of the bubble. The lower dashed curves give the volume of the first detached bubble of a compound bubble, and the intermediate dashed curves give the volume of the first detached couple when double coalescence occurs. The dotted horizontal line is the dimensionless volume 47.497 computed in (Longuet-Higgins et al. 1991) for quasi-static detachment at $B = 0.1$. For comparison, notice that the Fritz's dimensionless volume for $B = 0.1$ is $V_F = \frac{2\pi}{B} = 62.83$. The dotted lines at the right correspond to volumes proportional to $We^{3/5}$ (Corchero et al. 2006)

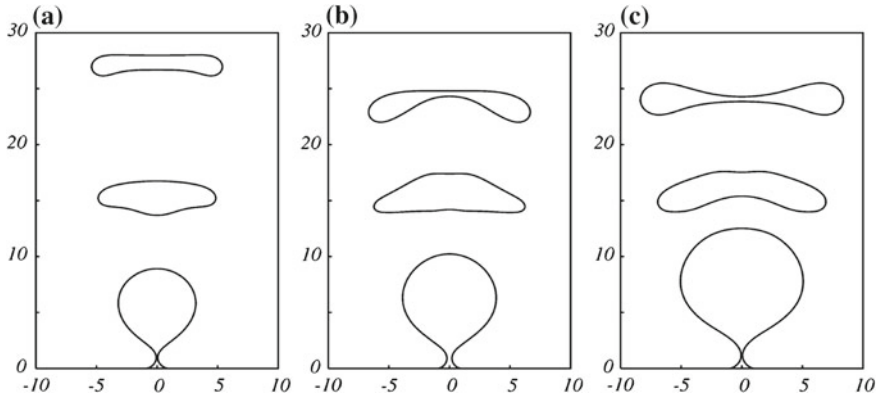


Fig. 4 Periodic generation of single bubbles for $B = 0.1$ and $We^{1/2} = 10$ (a), 20 (b), and 40 (c)

3 Equations for Bubbles Growing in Non-confined and Confined Viscous Liquid

The case of bubble generation in very viscous liquids is of interest in connection with polymer melts (Bird et al. 1987) and molten glasses and magmas (Sahagian 1985; Manga and Stone 1994), for example, but it has been comparatively less studied. Using a balance of buoyancy and viscous forces on the surface of each bubble,

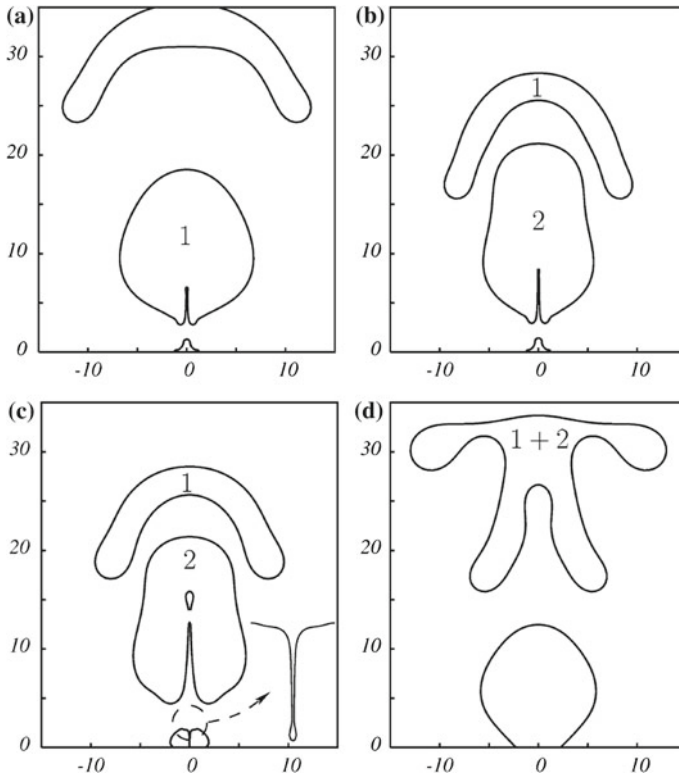


Fig. 5 Four snapshots of the generation of a (*double*) compound bubble for $B = 0.1$ and $We^{1/2} = 100$. **a** $t = 13.77$, immediately after the detachment of the leading bubble; **b** $t = 25.34$, immediately after the detachment of the trailing bubble; **c** $t = 25.64$, immediately after breakup of the thin upward jet; **d** $t = 33.68$, immediately after coalescence of the two bubbles. Times are non-dimensionalized with the capillary time $(\rho a^3/\sigma)^{1/2}$ and measured from the detachment of the bubble preceding bubble 1 in (a). The period of the process is 25.34. Notice the weeping in (c) and the displacement of the contact line away from the orifice in (c) and (d)

Davidson and Schuler (1960) proposed that the volume of the bubbles injected in a very viscous quiescent liquid increases as the $3/4$ power of the gas flow rate and is independent of the radius of the injection orifice. This estimate is intended to apply for high gas flow rates, for which the effect of the surface tension acting across the contact line of the attached bubble with the solid surface of the orifice is negligible. At very small flow rates, on the other hand, viscous forces are negligible during most of the growth of the bubble, whose shape is determined by a hydrostatic balance of buoyancy and surface tension. Longuet-Higgins et al. (1991) computed the equilibrium shapes of attached bubbles and the volume at which equilibrium state is not possible anymore and the bubble should detach. In orders of magnitude, the volume of the bubble at detachment, V , is given in this small-flow-rate regime by the hydrostatic balance $\rho g V \sim \sigma a$, or $V/a^3 \sim 1/B$ in dimensionless terms.

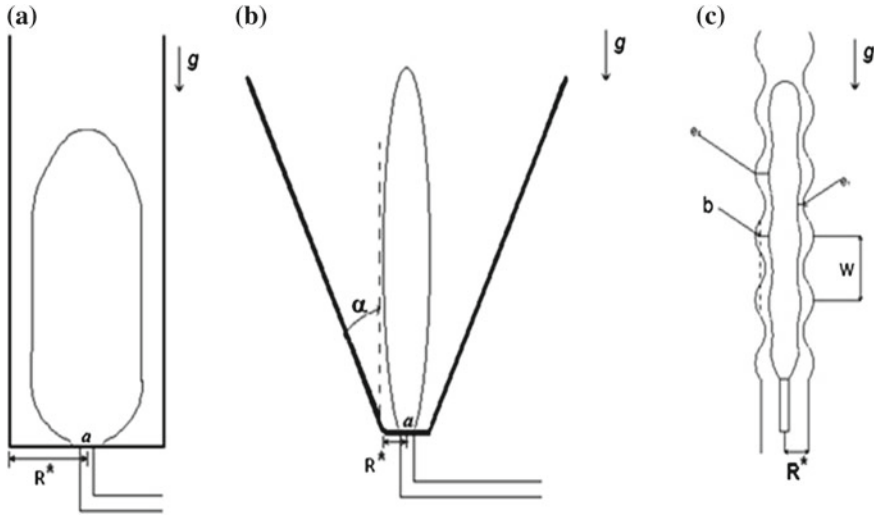


Fig. 6 Two-dimensional projections of the reservoirs symmetrical to the gas injection needles. Three different geometries are considered for bubbles growth in viscous fluids

Here ρ is the density of the liquid, σ is the liquid–gas surface tension, a is the radius of the injection orifice, g is the acceleration due to gravity, and B is de Bond Number (1).

A constant flow rate Q of an incompressible gas of negligible density and viscosity is injected into a liquid of density ρ and viscosity μ initially at rest in a reservoir under the action of the gravity. The gas is injected through a circular orifice of radius a at the center of the base of radius R^* of the reservoir. The lateral wall of the reservoir may be cylindrical, cylindrical corrugated or conical, making an angle θ to the vertical, as sketched in Fig. 6. The gas accumulates in a bubble attached to the base of the reservoir. The volume of this bubble increases with time until it detaches and begins to ascend in the liquid, being replaced by a new attached bubble. The effect of the inertia is assumed to be negligible in the motion induced in the liquid by the growth and displacement of the bubbles. A sufficient condition for the effect of the inertia to be negligible is that $Re = \frac{\rho Q}{\mu R_b} \ll 1$ (Wong et al. 1998; Higuera 2005; Ajaev and Homsy 2006). Here R_b is the characteristic radius of the detaching bubble or of its upper cap.

The model used here is valid to understand the bubble formation in a very viscous liquid in confined axisymmetric geometries (López-Villa et al. 2011). The equations of continuity and Stokes have the following dimensionless forms, respectively

$$\nabla \cdot \mathbf{v} = 0, \quad (5)$$

$$0 = -\nabla p + \nabla^2 \mathbf{v} - B \mathbf{i} \quad (6)$$

Here distances and times are scaled with the radius of the orifice a and the viscous time $\mu a / \sigma$, respectively, p is the pressure, v is the velocity field: $\mathbf{v} = \mathbf{v}^* \sigma / \mu$, \mathbf{i} is the normal vector pointing in the upward direction (x is the vertical coordinate).

When the bubble grows the dimensionless gas flow rate Q is constant and the capillary number is a dimensionless flow rate

$$Ca = \frac{\mu Q}{\sigma a^2}. \quad (7)$$

When a bubble is formed in the liquid, a free surface of the form $f(\mathbf{x}, t) > 0$ exists. Equations (5) and (6) must be solved with the boundary conditions

$$\frac{Df_i}{Dt} = 0, \quad (8)$$

$$-p\mathbf{n}_i + \tau' \cdot \mathbf{n}_i = (\nabla \cdot \mathbf{n}_i - p_{gi})\mathbf{n}_i, \quad (9)$$

on the surfaces of the i -th bubbles and

$$\mathbf{v} = 0 \quad (10)$$

on the inner cylinder's surface ($r = R^*$), and at infinity, because the fluid does not move there. Moreover, the pressure far from the bubble must satisfy

$$p + Bx = \text{constant}. \quad (11)$$

The uniform pressure of the gas in the bubble, $p_g(t)$, is determined using the conditions that the volume V of the bubble increases linearly with time at a rate equal to Q for the attached bubble. In dimensionless variables,

$$\frac{dV}{dt} = Ca. \quad (12)$$

In above equations $\mathbf{n} = \nabla f / |\nabla f|$ is a unit vector normal to the surface of the bubble, $\tau' = \nabla \mathbf{v} + (\nabla \mathbf{v})^T$ is the dimensionless viscous stress tensor, x and r are distances along the axis of the reservoir and normal to it. The condition (8) shows that the surfaces of the bubbles are fluid surfaces which separate the liquid from the gas, and therefore there is no mass exchange through them. The condition (9), in turn, expresses the balance of the stress acting on surfaces of the bubbles.

If the gas pressure p_{gi} is known in each bubble, the Eqs. (5) and (6) together with the boundary conditions determine velocity fields and fluid pressure, and in particular, the velocity on the surface of each bubble. To determine the pressures and complete the formulation of the problem conditions to be used, the volumes of the released bubbles ($i > 1$) are assumed constant and equal to the volumes at the instant of their release.

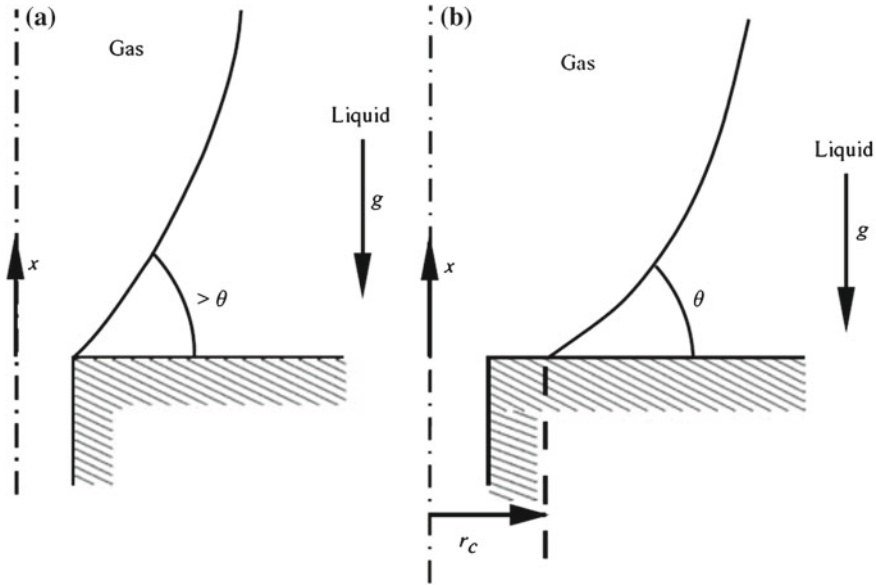


Fig. 7 Details of the contact line with two possibilities of line of contact of the bubble adhesion

An additional condition is needed at the contact line of the growing bubble with the solid. Here the contact line will be taken to coincide with the edge of the orifice when the angle of the liquid–gas surface with the horizontal bottom is larger than the contact angle (i.e. when $-\mathbf{n}_{x0} < \cos \theta$, where \mathbf{n}_{x0} is the vertical component of the unit normal vector \mathbf{n}_0 to the attached bubble), and to spread away from the orifice, with the liquid–gas surface making a constant contact angle with the solid bottom ($-\mathbf{n}_{x0} < \cos \theta$) otherwise (Higuera 2005); see Fig. 7.

The line of contact of the bubble adhered ($i = 1$) with the reservoir base is a circle which may coincide with the edge of the orifice or move to a position $r > 1$ to be determined. Figures 7a and b illustrate both possibilities. In the first case, the radius of the contact line coincides with the hole edge, $r = 1$. In the second case, the angle which the bubble surface makes with the base of the reservoir must match the contact angle θ , which is a property of the liquid and the material of the shell.

Then the problem contains five dimensionless parameters which are the Bond number, B , the capillary number Ca , the dimensionless radius of the base of the reservoir $R = R^*/a$, semiangle of the conical base α and the contact angle θ of the liquid with the base (Fig. 7).

The set of equations given above will satisfy the outflow boundary conditions at infinity, the non-slip conditions on walls, and the quasi-static pressure balance. The evolution of the free surface (bubble shapes) is given by the solution of Eq. (8), under a fourth order Runge-Kutta scheme, which is attained after solving the hydrodynamic problem, imposed by Eqs. (5) and (6), by using the BEM method (López-Villa et al. 2011). The reservoir configurations are shown in Fig. 6.

4 Method for Numerical Solution

We seek for axisymmetric solutions of the Eqs. (5)–(12). We use a standard boundary elements method (Pozrikidis 1992, 2002) to solve the Stokes Eqs. (5) and (6) with the boundary conditions (9)–(11), and a fourth order Runge-Kutta method to calculate the evolution of free surface f given by (8).

4.1 History

After three decades of development, the boundary element method (BEM) has found a firm footing in the arena of numerical methods for partial differential equations. Compared to more popular numerical methods, such as the Finite Element Method (FEM) and the Finite Difference Method (FDM), both of which can be classified as the domain methods, the BEM distinguishes itself as a boundary method, meaning that the numerical discretization is conducted at reduced spatial dimension. For example, for problems in three spatial dimensions, the discretization is performed on the bounding surface only; and in two spatial dimensions, the discretization is on the boundary contour only. This reduced dimension leads to linear systems, less computer memory requirements, and more efficient computation. These advantages are most notorious when the domain is unbounded. Unbounded domain needs to be truncated and approximated in domain methods. The BEM, on the other hand, automatically models the behavior at infinity without the need of deploying a mesh to approximate it. In the modern day industrial settings, mesh preparation is the most intensive labor and the most costly portion in numerical modeling, particularly for the FEM. Without the need of dealing with the interior mesh, the BEM is more cost effective in mesh preparation. For problems involving moving boundaries, the adjustment of the mesh is much easier with the BEM. With these advantages, the BEM is indeed an essential part in the repertoire of the modern day computational tools (Alexander and Daisy 2005).

One can view BEM as the numerical implementation of boundary integral equations based on Green's formula, in which the piecewise element concept of the FEM is utilized for the discretization.

4.2 BEM in Axisymmetric Domains

In this section we describe the standard boundary elements method for three-dimensional flow in an axisymmetric domain. Our goal is to reduce the boundary integral equation to a one-dimensional equation, or a system of one-dimensional equations, over the trace of the boundaries in an azimuthal plane. First, the Green's functions of Stokes flow represent solutions of the continuity equation $\nabla \cdot \mathbf{v} = 0$ and the singularly forced Stokes equation

$$-\nabla P + \mu \nabla^2 \mathbf{v} + g \delta(\mathbf{x} - \mathbf{x}_0) = 0, \quad (13)$$

where $\delta(\mathbf{x} - \mathbf{x}_0)$ is Dirac's delta function in three dimensions, g is an arbitrary constant, \mathbf{x}_0 is an arbitrary point. Introducing the Green's function G for three dimensions, we write the solution of (13) in the form

$$\mathbf{u}_i = \frac{1}{8\pi\mu} G_{ij}(\mathbf{x} - \mathbf{x}_0) g_j, \quad (14)$$

here \mathbf{x} is the observation or field point. Physically, (14) expresses the velocity field due to a concentrated point force of strength g placed at the point \mathbf{x}_0 , and may be identified with the flow produced by the slow settling of a small particle. In the literature of boundary integral methods, the Green's function may appear under the names fundamental solution or propagator (Pozrikidis 1992).

It is convenient to classify the Green's functions into three categories depending on the topology of the domain of flow. First, we have the free-space Green's function for infinite unbounded flow; second, the Green's functions for infinite or semi-infinite flow that are bounded by a solid surface; and third, the Green's function for internal flow are completely confined by solid surfaces. The Green's functions in the second and third categories are required to vanish over the internal or external boundaries of the flow. As the observation point \mathbf{x} approaches the pole \mathbf{x}_0 all Green's functions exhibit singular behavior and, to leading order, behave like the free-space Green's function. The Green's functions for infinite unbounded or bounded flow are required to decay at infinity at a rate equal to or lower than that of the free-space Green's function.

$$\frac{\partial G_{ij}(\mathbf{x} - \mathbf{x}_0)}{\partial x_i} = 0, \quad (15)$$

for (14).

Integrating (15) over a volume of fluid that is bounded by the surface D and using the divergence theorem, we find

$$\int_D G_{ij}(\mathbf{x} - \mathbf{x}_0) n_i(\mathbf{x}) dS(\mathbf{x}) = 0, \quad (16)$$

independently of whether the pole \mathbf{x}_0 is located inside, right on, or outside D .

The vorticity, pressure, and stress fields associated with the flow (15) may be presented in the corresponding forms:

$$\omega_i = \frac{1}{8\pi\mu} \Omega_{ij}(\mathbf{x} - \mathbf{x}_0) g_j, \quad (17)$$

$$P = \frac{1}{8\pi\mu} \mathbf{p}_j (\mathbf{x} - \mathbf{x}_0) g_j, \quad (18)$$

$$\tau_{ij} = \frac{1}{8\pi\mu} \mathbf{T}_{ijk} (\mathbf{x} - \mathbf{x}_0) g_j, \quad (19)$$

where $\mathbf{\Omega}$, \mathbf{p} , and \mathbf{T} are the vorticity tensor, pressure vector, and stress tensor associated with the Green's function. The stress tensor \mathbf{T} , in particular, is defined as

$$\mathbf{T}_{ijk} (\mathbf{x} - \mathbf{x}_0) = -\delta_{ik} \mathbf{p}_j (\mathbf{x} - \mathbf{x}_0) + \frac{\partial \mathbf{G}_{ij}}{\partial x_k} (\mathbf{x} - \mathbf{x}_0) + \frac{\partial \mathbf{G}_{ij}}{\partial x_i} (\mathbf{x} - \mathbf{x}_0). \quad (20)$$

It will be noted that $\mathbf{T}_{ijk} = \mathbf{T}_{kji}$ as required by the symmetry of the stress tensor $\boldsymbol{\tau}$. When the domain of flow is infinite, we require that all $\mathbf{\Omega}$, \mathbf{p} , and \mathbf{T} vanish as the observation point is moved to infinity.

Considering first axisymmetric flow with no swirling motion, we observe that in cylindrical coordinates, none of the boundary variables is a function of the azimuthal angle. This reduces the number of variable.

In the problem of bubble generation, the contours are the surfaces of the bubbles and the solid surfaces of the reservoir, which are all surfaces of revolution. The unknowns involved in the formulation of the boundary element are the velocities of fluid particle that define surfaces of the bubbles and the stresses on the vessel wall.

We introduce the dimensionless driving pressure $P = p + Bx$, which allows us to write the Stokes Eq. (6) as

$$0 = -\nabla P + \nabla^2 \mathbf{v} = \nabla \cdot \boldsymbol{\tau}, \quad (21)$$

where $\boldsymbol{\tau} = -P\mathbf{I} + \boldsymbol{\tau}'$ is a modified stress tensor, with fluid pressure replaced by the driving pressure. The stress of liquid on the surface of the i -th bubble, given by left hand side of (9), is then

$$-p\mathbf{n}_i + \boldsymbol{\tau}' \cdot \mathbf{n}_i = -P\mathbf{n}_i + \boldsymbol{\tau}' \cdot \mathbf{n}_i + Bx\mathbf{n}_i. \quad (22)$$

We will use the notation $\mathbf{f} = \boldsymbol{\tau} \cdot \mathbf{n}$ for the modified stress on the limiting contour of the liquid, where \mathbf{n} is the normal to the contour directed towards the liquid. With this notation $-p\mathbf{n}_i + \boldsymbol{\tau}' \cdot \mathbf{n}_i = \mathbf{f} + Bx\mathbf{n}_i$ and the boundary condition (9) on the bubble, the i -th surface takes the form

$$\mathbf{f} = (\nabla \cdot \mathbf{n}_i - Bx - p_{gi}) \mathbf{n}_i. \quad (23)$$

Additionally, we use the Green's functions for axisymmetric flow, which are the solutions of Stokes equations in unlimited space (14) with the stresses concentrated on a circumference of radius r_0 centered at point \mathbf{x}_0 on the axis of symmetry. These forces can be either directed along the axis of symmetry or be in perpendicular to it, which gives rise to two distinct solutions whose velocity and motion pressure distributions denoted as $\mathbf{G}^x(\mathbf{x}, \mathbf{x}_0)$ and $\mathbf{P}^x(\mathbf{x}, \mathbf{x}_0)$ for axial force, and $\mathbf{G}^r(\mathbf{x}, \mathbf{x}_0)$ and

$\mathbf{P}^r(\mathbf{x}, \mathbf{x}_0)$ for a radial force. Here, $\mathbf{x} = (x, r_0)$ and $\mathbf{x} = (x, r)$ (a generic point) in cylindrical coordinates defined above. The equations to be solved to determine the Green's functions are

$$\nabla \cdot \mathbf{G}^x = 0, \quad 0 = -\nabla P^x + \nabla^2 \mathbf{G}^x + 8\pi \delta(x, x_0) \mathbf{e}_x, \quad (24)$$

and

$$\nabla \cdot \mathbf{G}^r = 0, \quad 0 = -\nabla P^r + \nabla^2 \mathbf{G}^r + 8\pi \delta(x, x_0) \mathbf{e}_r, \quad (25)$$

with the conditions $(\mathbf{G}^x, \mathbf{P}^x) \rightarrow 0$ and $(\mathbf{G}^r, \mathbf{P}^r) \rightarrow 0$ at infinity. In these equations \mathbf{e}_x , \mathbf{e}_r , are the unit vectors parallel and perpendicular to the axis of symmetry, respectively, δ is the Dirac function, and 8π factor is introduced by convention. We will also use the notation T^r and T^x for stress tensor of the solutions (24) and (25). These solutions are known and are given in Appendix A.

Given that $\nabla \cdot \mathbf{v} = \nabla \cdot \mathbf{G}^x = 0$ verifies that

$$\nabla \cdot (\mathbf{G}^x \cdot \boldsymbol{\tau} - \mathbf{v} \cdot T^x) = \mathbf{G}^x \cdot (\nabla \cdot \boldsymbol{\tau}) - \mathbf{v} \cdot (\nabla \cdot T^x).$$

Using (22) and (24) (i.e. $\nabla \cdot \boldsymbol{\tau} = 0$ and $\nabla \cdot T^x = 8\pi \delta(x, x_0) \mathbf{e}_x$) in the second term of the above equality, and by integrating the result over the volume occupied by liquid and using the Gauss theorem for flow in an axisymmetric domain and transforming the integral of the first member in a surface integral. Then in a line integral on the meridional section of the bubbles and the walls tube denoted as C , is obtained

$$\begin{aligned} - \int_C \mathbf{G}^x(\mathbf{x}, \mathbf{x}_0) \cdot \mathbf{f}(\mathbf{x}) r(\mathbf{x}) dl(\mathbf{x}) + \int_C \mathbf{v}(\mathbf{x}) \cdot T^x(\mathbf{x}, \mathbf{x}_0) \mathbf{n}(\mathbf{x}) r(\mathbf{x}) dl(\mathbf{x}) \\ = 8\pi r_0 v_x(\mathbf{x}_0), \end{aligned} \quad (26)$$

where $\mathbf{f}(\mathbf{x})$, $r(\mathbf{x})$ and $dl(\mathbf{x})$ are defined in a point \mathbf{x} in the contour C , which are, respectively, the distance from this point to the axis of symmetry, and the arc element on the boundary. Similarly,

$$\begin{aligned} - \int_C \mathbf{G}^r(\mathbf{x}, \mathbf{x}_0) \cdot \mathbf{f}(\mathbf{x}) r(\mathbf{x}) dl(\mathbf{x}) + \int_C \mathbf{v}(\mathbf{x}) \cdot T^r(\mathbf{x}, \mathbf{x}_0) \mathbf{n}(\mathbf{x}) r(\mathbf{x}) dl(\mathbf{x}) \\ = 8\pi r_0 v_r(\mathbf{x}_0), \end{aligned} \quad (27)$$

In the derivation of (26) and (27) it is assumed that the circumference on which the force is applied is concentrated in the volume occupied by liquid. If not, the second members of these equations are null. The second integral on the left hand side of (26) and (27) diverge when the point tends \mathbf{x}_0 to the contour C . A detailed calculation, deforming the contour in the vicinity of \mathbf{x}_0 (see, for example, Pozrikidis 1992) shows that for $\mathbf{x}_0 \in C$,

$$\mathbf{v}_j(\mathbf{x}_0) = -\frac{1}{4\pi} \int_c G_k^j(\mathbf{x}, \mathbf{x}_0) f_k(\mathbf{x}) \frac{r}{r_0} dl + \frac{1}{4\pi} \int_c^{PV} v_k(\mathbf{x}) T_{kl}^j(\mathbf{x}, \mathbf{x}_0) n_l(\mathbf{x}) \frac{r}{r_0} dl, \quad (28)$$

where PV indicates the principal value of the integral and subscripts notation was used with or $(i, j, k) = x$ or r , for compactness.

Equation (28) is a ratio between speeds and stresses on the contour surface C domain occupied by the liquid. If stresses \mathbf{f} were known at all points of C , this equation lets calculate the velocity of the liquid in C . Similarly, if in \mathbf{v} C is known the equation allows compute \mathbf{f} (except for an undetermined constant P ; see Pozrikidis 2002).

In the problem of bubble generation, $\mathbf{v} = 0$ on the solid surfaces wetted by the liquid. The velocity of liquid on the bubbles is unknown, however, the modified stress can be obtained by using Eq. (23). Moreover, suppose all bubble stresses are known at a certain instant. The stress given by Eq. (23) would then be known if p_{gi} were known. In this case, the solution of (28) determines the velocity of the liquid on the surfaces of the bubbles and stresses on the solid surfaces. With p_{gi} unknown, the stress on the bubble i is the sum of a known stress $(\nabla \cdot \mathbf{n}_i - B_x) \mathbf{n}_i$, and a normal uniform stress, $-p_{gi} \mathbf{n}_i$.

Given the linearity of the Eq. (28), the velocity on the surfaces of bubbles and stress on solid surfaces are

$$\mathbf{v} = \mathbf{v}^0 + \sum_i \mathbf{v}^i(p_{gi}) \quad \text{and} \quad \mathbf{f} = \mathbf{f}^0 + \sum_i \mathbf{f}^i(p_{gi}) \quad (29)$$

where \mathbf{v}^0 and \mathbf{f}^0 are the velocity and the stress calculated for all $p_{gi} = 0$ in (18), and \mathbf{v}^i and \mathbf{f}^i are the velocity and the stress calculated for $\mathbf{f} = 0$ on all surfaces of the bubbles except the bubble i , where $\mathbf{f} = -\mathbf{n}_i$.

Equation (28) provide the solution of (27) in terms of the pressures of the gas in the bubbles, p_{gi} . We now need to establish equations to calculate these pressures. These equations express the conditions (12) and the volumes of the bonded bubbles released ($i > 1$) are constant and the volume of the bubble grows linearly with time. In terms of the velocities of the liquid (28), the rate of change of volume of the bubble j is

$$\frac{dV_j}{dt} = 2\pi \int_{c_j} \mathbf{v} \cdot \mathbf{n}_j r dl = a_{j0} + \sum_i a_{ji} p_{gi}, \quad (30)$$

where C_j is the contour of the bubble, and a_{j0} and a_{ji} are easily calculated from velocities \mathbf{v}^0 and \mathbf{v}^i . Thus, the linear equations are obtained

$$a_{10} + \sum_i a_{1i} p_{gi} = Ca \quad \text{and} \quad a_{j0} + \sum_i a_{ji} p_{gi} = 0 \quad \text{for } j > 1, \quad (31)$$

which determine p_{gi} and complete the solution (28) given the surfaces of the bubbles.

To complete the formulation of the problem, we must consider the conditions (8), expressing the surface of each bubble moving with the local velocity the liquid. The position $\mathbf{x}(t)$ of a fluid particle on the surface of a bubble satisfies

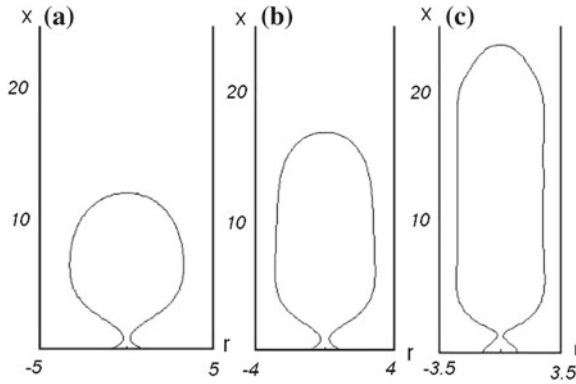


Fig. 8 Meridional sections of bubbles which are about to detach from the base of a cylindrical reservoir for $B = 0.2$, $Ca = 10$, and $R = 5$ (a), 4 (b) and 3.5 (c)

$$\frac{dx}{dt} = v(x, t), \quad (32)$$

where $v(x, t)$ is the solution of (28)–(31) at the point x on the surface in the time t .

To solve numerically the integral Eq. (28), the contours of the bubbles and solid surfaces must be discretized. This is done using N_i nodes distributed uniformly on the bubble boundary i and N_d nodes on the base of the reservoir, distributed non-uniformly with space increasing with distance from the axis of symmetry. The integrals in (28) are calculated using a Gaussian integration with six points allocated in the interval between each pair of nodes. The surface is discretized with a finite number of nodes that move as material particles. Numerical tests conducted with different numbers of nodes show that 120 nodes give sufficient resolution.

The value $\theta = 45^\circ$ has been used for the contact angle in the computations that follow. Numerical computations with other values θ of show that the effect of the contact angle on the volume of the bubbles is small as far as $\theta < 90^\circ$.

5 Numerical Results

From the numerical solutions a set of important results are achieved. These results are compared with experiments qualitatively, where the effects of reservoir geometry and film thickness is studied.

5.1 Cylindrical Reservoir

Some numerical computations have been carried out to study the growth and detachment of a bubble in a cylindrical reservoir and validate it with experiments. Figure 8

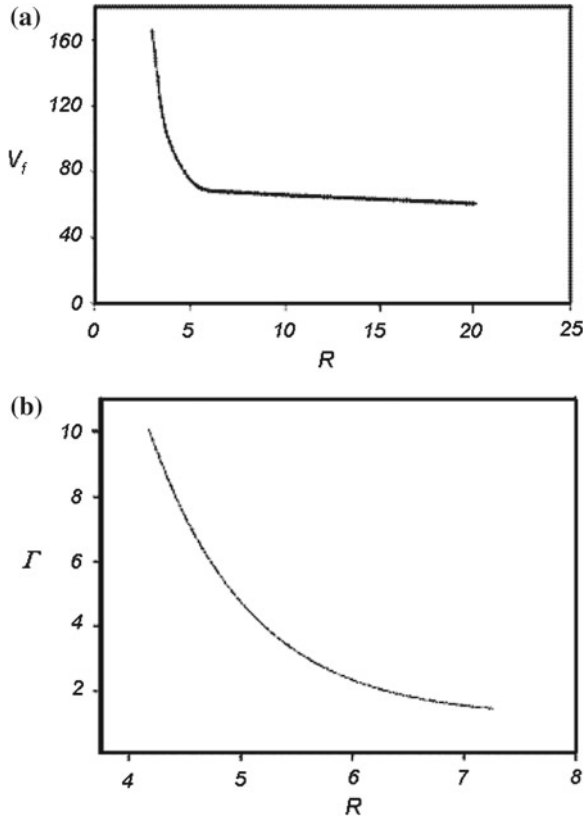


Fig. 9 Plots of **a** volume V_f and **b** aspect ratio Γ of a bubble at detachment from the base of the cylindrical reservoir as functions of it R for $B = 0.2$, and $Ca = 10$

shows a bubble which is about to detach from the base of the reservoir for $B = 0.2$, $Ca = 10$, and the three values $R = 5, 4$ and 3.5 of the dimensionless radius of the reservoir. Figure 9 shows plots of V_f , volume of detachment, and the aspect ratio Γ of the bubble (defined as the ratio of the height to the maximum diameter of the bubble) as functions of R .

The finite radius of the reservoir affects only the high-flow-rate regime for the values of B and R used here. The decrease of Γ with increasing R in Fig. 9b is in qualitative agreement with the estimate $L_f/R \sim Ca/(BR^4)$ for columnar bubbles. The decrease of V_f in Fig. 9a also agrees with the previous estimates, according to which the ratio of the volume of a columnar bubble to the volume of a bubble detaching in an infinite reservoir is of order $(Ca/B)^{1/4}/R$ for Ca/B large compared to R^4 . Figure 9 shows V_f as a function of Ca for $B = 0.2$ and three values of R . The nearly linear increase of V_f agrees with the estimate $V_f \sim Ca/B$. Notice, in comparison, that $V_f \sim (Ca/B)^{3/4}$ for a bubble in an infinite reservoir.

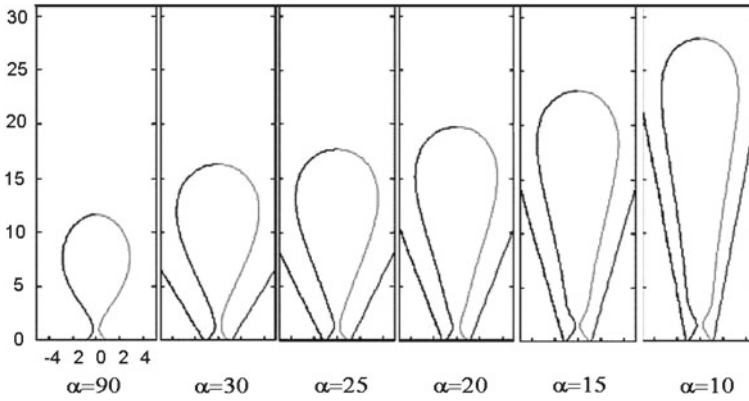


Fig. 10 Meridional sections of bubbles growing in cones which are about to detach from the base of a conical reservoir for $B = 0.2$, $Ca = 50$, $R = 1.2$, and various values of α

Numerical computations also show (results not displayed) that the center of mass of a columnar attached bubble rises linearly with time during the growth of the bubble, and that the velocity of the center of mass is nearly constant, except in the early stages of the process, when the bubble is still small compared to the radius of the tube.

5.2 Conical Reservoirs

Figure 10 shows the shape of a bubble which is about to detach from the base of a conical reservoir for $B = 0.2$, $Ca = 50$, $R = 1.2$, and various values of the semi-angle of the cone, α , and Fig. 11 shows the volume V_f and the aspect ratio Γ of the detaching bubble as functions of α and different values of B and Ca . As it can be seen, the volume of the bubble always increases as the angle of the cone decreases, the effect being more pronounced for small values of the Bond number, for which the bubble is larger and therefore more easily affected by the wall of the reservoir. Figure 11a displays an important result of this work, namely, that at low Bond numbers and high capillary numbers, the volume of the bubbles can be easily controlled through the angle of the cone without having to change the flow rate. This is a desirable feature in some applications.

These results can be rationalized by means of a straightforward extension of the estimations of the previous section for the high-flow-rate regime in cylindrical reservoirs. Figure 10 shows that the bubbles in conical reservoirs are columnar for moderately small values of α , with a cap that increases linearly with its height above the bottom of the reservoir. (See also Fig. 11b; the bubble is slender for smaller than 30°).

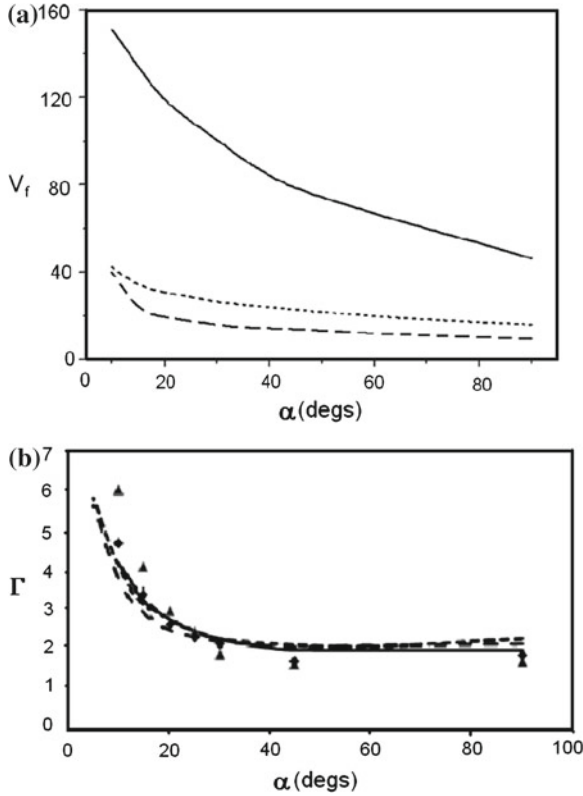


Fig. 11 Plots of **a** volume V_f and **b** aspect ratio Γ of a bubble at detachment from the base of a conical reservoir as functions of α , for $R = 1.2$ and $(B, Ca) = (0.2, 10)$ (solid), $(2, 10)$ (dashed), and $(2, 20)$ (dotted). Symbols in panel (b) show the values of Γ measured experimentally for $B = 0.0176$ (\blacktriangle) and $B = 0.15$ (\blacklozenge), with $Ca = 50.78$ and $R = 1.2$

5.3 Corrugated Pipes

For the corrugated cylinder case, the numerical study was done to understand how corrugations affect the bubble shape. We tried different number of nodes distributed along the tube walls, and found that as in the case of the smooth walls, the number of nodes has no importance on qualitative behavior.

Figure 12 shows differences between bubbles formed in tubes with several corrugation wavelengths in the viscous case, and in Fig. 13 the cases in the inviscid approximation are shown with different amplitudes of corrugation. Figure 13 shows that the film thickness is small in the case of a small capillary number.

In Figs. 14 and 15 we observe the bubbles detachment process and a possible application to understand the foams formed in viscous fluids in porous media (Kovscek et al. 1995; Hirasaki et al. 2006).

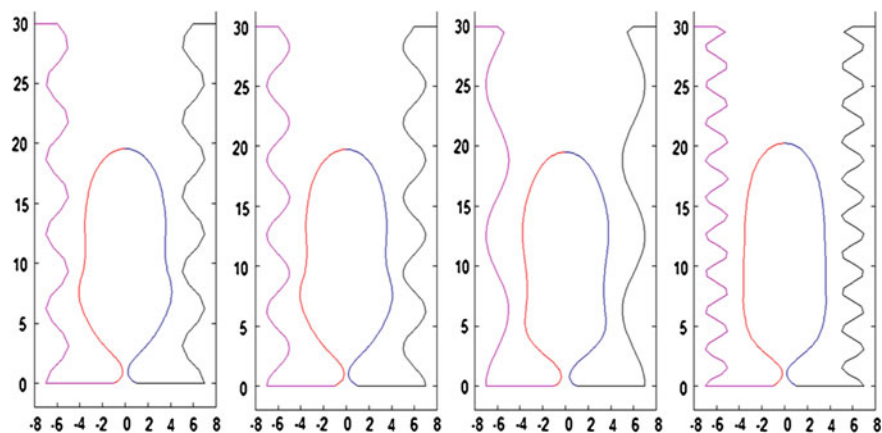


Fig. 12 Bubble shapes in corrugated cylinders of same amplitude but different wavelengths of the corrugations. The conditions are for viscous liquid and $Ca = 25$, $B = 0.2$

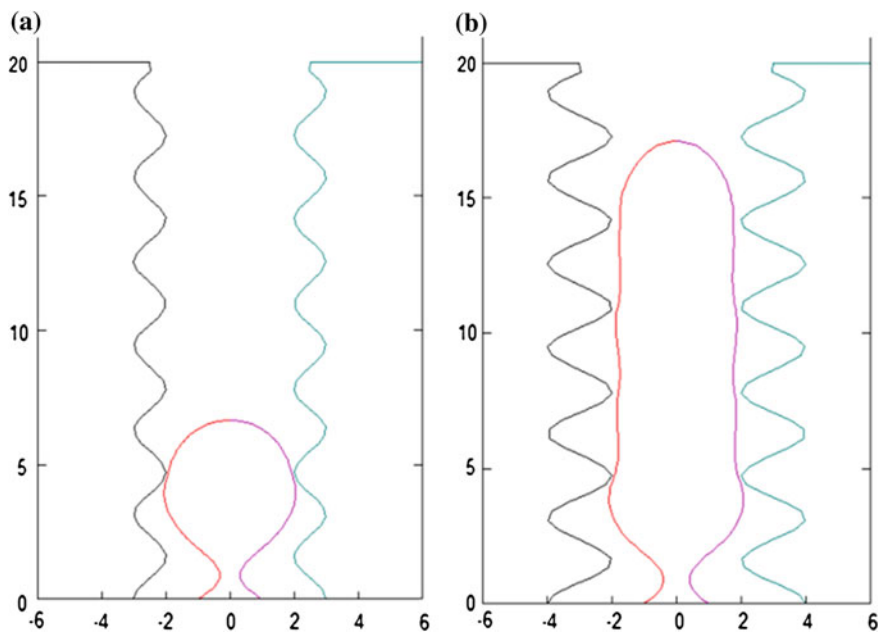


Fig. 13 Bubble shapes in corrugated cylinders of same wavelengths but different amplitudes. **a** Bubbles growing in nearly inviscid liquid, i.e., $Ca = 0.1$ and $B = 0.2$. In **b** $Ca = 1$ and $B = 0.2$. Notice that the thickness of the film in both cases is very thin

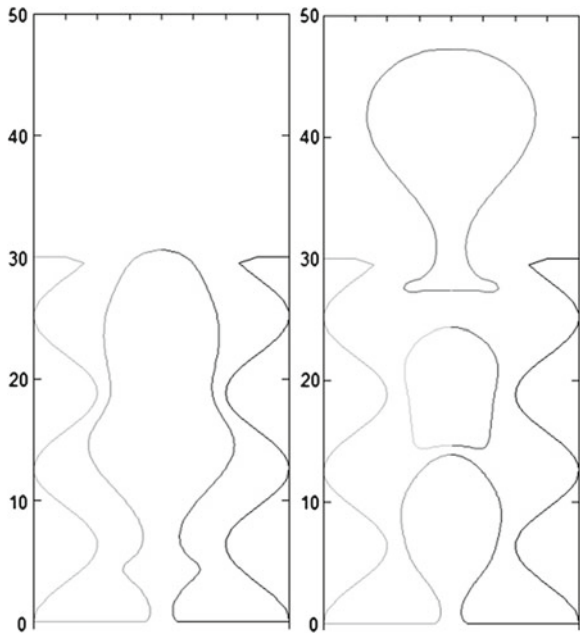


Fig. 14 Details of the bubble detachment process and the effect of the tube wall

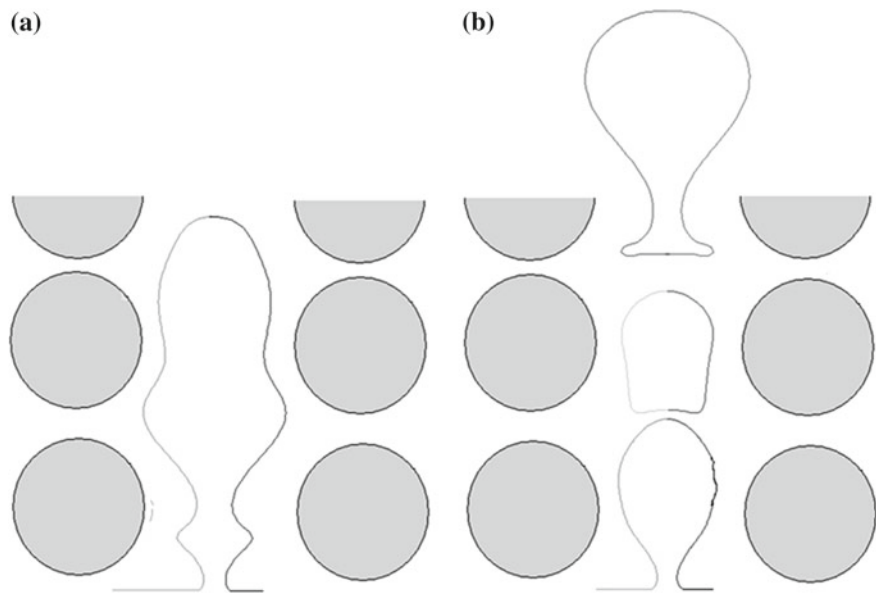


Fig. 15 Bubble shapes in the corrugated pipe compared to a bubble growing in a porous medium

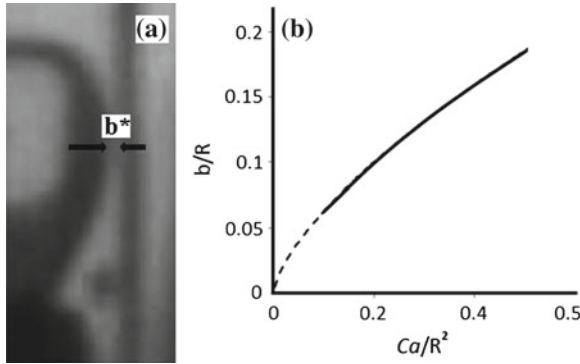


Fig. 16 Bubble in a vertical tube (a). Notice the existence of a film of thickness b^* . b Plot of the scaled dimensionless film thickness b/R as a function of the scaled capillary number Ca/R^2

5.4 The Film Thickness

In Fig. 16a it is shown that during the bubble growth in the pipe there is an annular film of thickness b^* . In a classical study of the lubrication theory, the dimensionless thickness of the film scales as

$$\frac{b}{R} \sim \left(\frac{Ca}{R^2} \right)^{\frac{2}{3}}, \quad (33)$$

which is valid whenever $Ca \rightarrow 0$ and R and the Bond number are also small. In Fig. 16b a plot obtained from the numerical computations that obeys the relation (33) is given. In such a plot the continuous curve was obtained through our numerical solution. Meanwhile, the dashed part of the curve only shows the trend given by Eq. (33) but was numerically inaccessible. Despite it, in this case, clearly $b \rightarrow 0$ if $Ca \rightarrow 0$. Physically the condition $Ca \rightarrow 0$ implies that the bubble in an inviscid liquid touches the inner solid wall.

Figure 17a shows some bubble profiles: in this case they were obtained for low capillary numbers and it is evident that the film thickness tends towards zero for small values of Ca and R . It can also be seen that the profiles show some “corrugations”, this is because they become unstable when the height of the tubes is very large compared with the tube radius, *i.e.* in this case height of the tube is 30 times the radius. In experiments it was observed that when $Ca \ll 1$ the small bubble profiles are unstable.

Moreover, very different results were obtained when the film thickness was computed for very viscous liquids, *i.e.*, $Ca \gg 1$ in the limit of low Bond number. In Fig. 17b it is possible to notice that the film thickness tend towards a constant value when the capillary number increases. In Fig. 18 it is sketched how $b \rightarrow \text{constant}$ for $Ca \gg 1$. In dimensional terms the actual thickness of the annular film, $b^* \rightarrow 1.5a^*$,

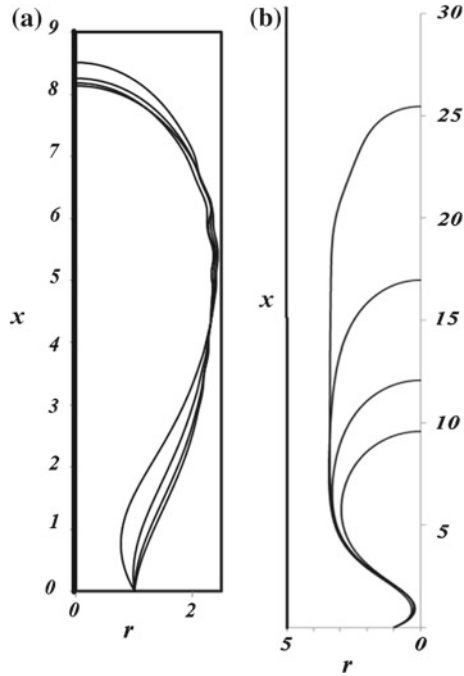


Fig. 17 Bubble shapes in cylinders filled with **a** liquid of low viscosity and **b** with very viscous liquid. In **a** the height and the film thickness between the bubble and the wall diminishes when $Ca \rightarrow 0$ ($Ca = 0.4, 0.3, 0.2$ and 0.1). In **b** the film thickness $b \rightarrow \text{constant}$, for $Ca \gg 1$. The larger bubble corresponds to $Ca = 35$; other cases are $Ca = 20, 10$ and 5 . The dimensionless pipe radius was $R = 5$

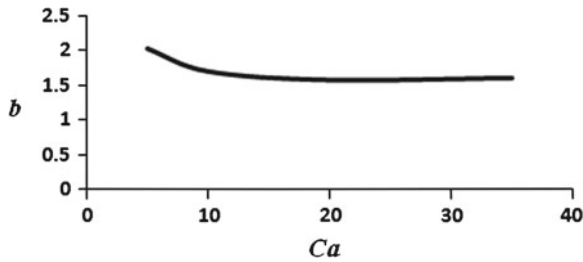


Fig. 18 Plot of the thickness of the annular film, b , as a function of the capillary number, Ca . Notice that $b \rightarrow \text{constant}$ for $Ca \gg 1$

i.e., the lower value of b^* is 1.5 times the radius of the gas injection orifice. Physically, this condition is attained in very viscous liquids or at very large gas flow rates.

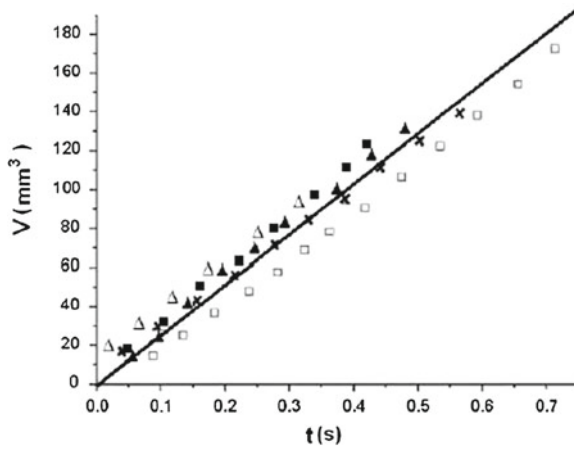


Fig. 19 Volume of a bubble attached to the base of a conical reservoir filled with glycerine as a function of time during the growth of the bubble for $B = 0.0176$, $R = 1.2$, and different values of the semi-angle of the cone. $\alpha = 10^\circ$ (\square), 20° (\times), 25° (\blacktriangle), 30° (\blacksquare) and 90° (\triangle)

6 Experiments

A series of experiments have been carried out to study the growth and detachment of bubbles in very viscous liquids. Glycerine and a silicone oil have been used in different experiments. The properties of glycerine at 25° are: density $\rho = 1260 \text{ kg/m}^3$, viscosity $\mu = 7.9 \times 10^{-1} \text{ N s/m}^2$, and surface tension $\sigma = 6.3 \times 10^{-2} \text{ N/m}$. The properties of the silicone oil at the same temperature are: density $\rho = 971 \text{ kg/m}^3$, viscosity $\mu = 9.71 \times 10^{-1} \text{ N s/m}^2$. In each experiment, a large open container with an horizontal bottom where a circular orifice of radius $a = 0.3 \text{ mm}$ has been drilled was filled with the chosen liquid to a height of 100 mm.

A glass tube of inner radius $R^* = 3.2 \text{ mm}$ was set vertically and concentrically with the orifice to form a cylindrical reservoir. Conical reservoirs of various angles were formed by carefully inserting cones made of acetate sheet concentrically with the orifice. Air was pumped through a capillary tube 40 cm long and 0.6 mm of inner diameter which ends at the orifice in the bottom of the container. We found in a previous work (Corchero et al. 2006) that a length of 40 cm suffices to make the pressure drop in the air line it is large compared to the pressure variations in the bubble during the growth process and therefore ensure a constant flow rate in our experiments, which is one of the premises of the numerical work. To check that the flow rate is constant, the evolution of the attached bubble was video recorded; the contour of the bubble was extracted from the video images using a standard algorithm (Russ 2002) implemented in a home made code; and the volume of the bubble, $V(t)$, and the height of its center of mass, $x_{CM}(t)$, were computed assuming that the bubble is axisymmetric. Some sample plots of V as a function of time for a bubble growing in glycerine within conical reservoirs of various angles are shown

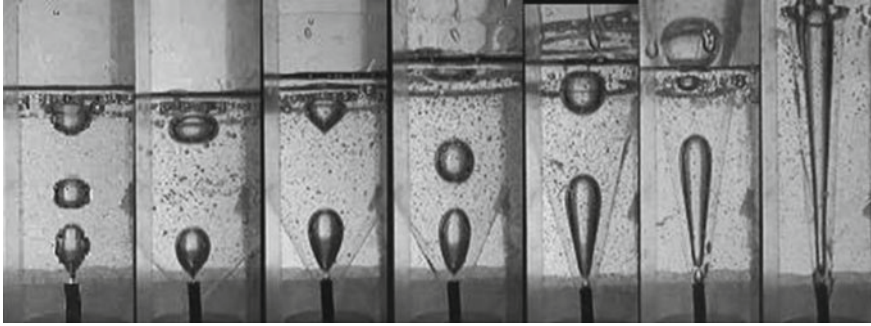


Fig. 20 Growth of bubbles at different angles of inclination α

in Fig. 19. The approximate linear variation of V with time shows that the flow rate is nearly constant and independent of the angle of the cone. The value of the flow rate determined by fitting a straight line to the experimental data of Fig. 19 is $Q = 364.5 \text{ mm}^3/\text{s}$. The same procedure was used to measure the flow rate of air injected into silicone oil and in cylindrical containers. The flow rate was found to be nearly constant in all cases.

Figure 20 shows the shapes of bubbles in glycerine which are about to detach from the injection orifice in conical reservoirs of various angles. Here $\alpha = 90^\circ$ corresponds to a bubble detaching in an infinite reservoir, and the shape of the bubbles begin to differ significantly from this case when α becomes smaller than about 30° . Coalescence between previously detached bubbles can be seen in some of the images. The presence of the conical wall of the reservoir increases the drag of the ascending bubbles, decreasing their velocity and apparently promoting coalescence. We plan to analyze this important aspect of the generation of bubbles in a future work. The gas flow rate in this sequence of experiments is that measured from Fig. 19. Values of the dimensionless parameters are $Bo = 0.0176$, $Ca = 50.78$ and $R = 1.2$.

The aspect ratio Γ of the bubbles in Fig. 20 and others was also extracted from the images and is included in Fig. 12b (triangles and diamonds), where it is compared to numerical results obtained for similar values of the dimensionless parameters. The comparison is reasonably good, though the experimental values of Γ increase with decreasing somewhat faster than the numerical values, and become larger than them for small values of α . We think that the difference is due to the vertical momentum injected with the gas, which was not taken into account in the numerical computations. The evolution of the center of mass of the bubble is shown in Fig. 21 and compared to numerical results. The nearly linear increase of x_{CM} with time is to be compared to the $x_{CM} \propto t^{1/3}$ evolution expected for a round bubble growing in an infinite reservoir (Davidson and Schuler 1960). The difference clearly shows the effect of the conical wall.

Only silicone oil was used in experiments with cylindrical reservoirs because glycerine tends to produce small bubbles that linger in the reservoir for a long time and interfere with the observation of the bubble attached to the orifice. Figure 22

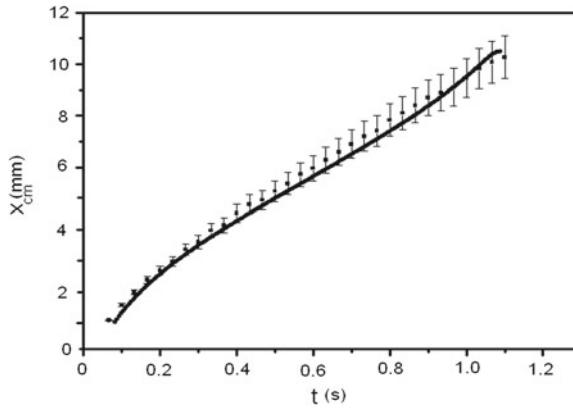


Fig. 21 Height of the center of mass of a bubble attached to the base of a conical reservoir as a function of time during the growth of the bubble for $Bo = 0.04$, $Ca = 70.23$, $R = 1.2$ and $\theta = 15^\circ$. Symbols are experimental results and the *solid curve* shows the results of the numerical computation

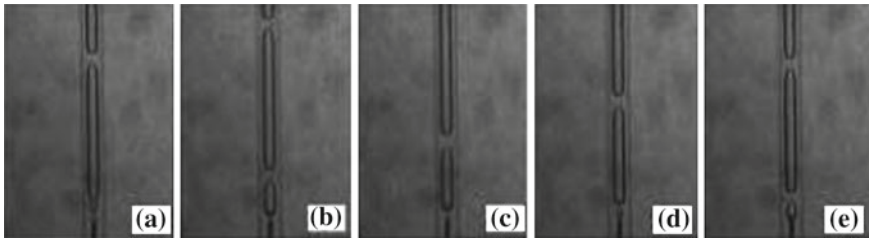


Fig. 22 Five equispaced images spanning the period of growth of a bubble attached to the base of a cylindrical reservoir for $B = 0.04$, $Ca = 209.94$ and $R = 10.66$. The period of bubbling is 1.33 s

shows five images equispaced in time that span the cycle of growth and detachment of a bubble. The flow rate of gas measured from the video record is $Q = 419.59 \text{ mm}^3/\text{s}$ in this experiment, and the period of bubbling is 1.33 s. Values of the dimensionless parameters are $Bo = 0.04$, $Ca = 209.94$ and $R = 10.66$. Figure 23 shows profiles bubbles formed into tubes with periodic corrugations $c = 7.33$, dimensionless radius $R^* = 3.7$, $Bo = 0.2$ to different capillary number.

7 Conclusions

The growth of a bubble due to the injection of a constant flow rate of a gas through an orifice in the horizontal base of a container filled with a very viscous liquid has been investigated numerically and experimentally in conditions in which nearby

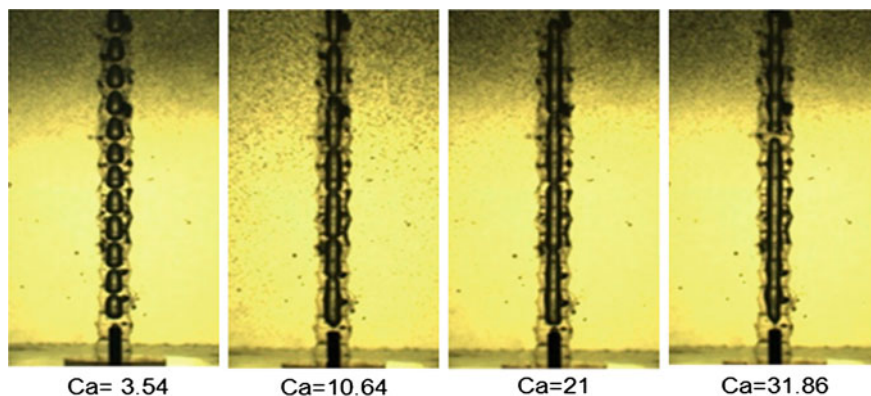


Fig. 23 dimension of profiles bubbles formed into tubes with periodic corrugations $c = 7.33$, dimensionless radius $R^* = 3.7$, $Bo = 0.2$ to different capillary number

solid walls partially confine the space where the bubble is allowed to grow. Conical, cylindrical and cylindrical with corrugations walls coaxial with the injection orifice have been used to allow easy control of the extent of the confinement by simply changing the angle of the cone or the radius of the cylinder or frequency in the corrugated case.

Numerical solutions of the Stokes equations for the liquid and the evolution equation for the free surface of the bubble show that the wall near the injection orifice may have an important effect on the shape of the bubble and its volume at detachment. Computations for small Bond numbers ($Bo = 0.2$) and moderately large capillary numbers (of the order of 10) made with BEM show that vertically elongated bubbles with volumes significantly larger than those of the round bubbles generated in the absence of walls are obtained when the radius of the cylindrical wall is smaller than about six times the radius of the orifice, or when the semi-angle of the cone is smaller than about 30° . The computed distributions of forces on the surface of the bubble and the wall suggest that buoyancy, viscous drag and viscous friction with the wall all play a role in the dynamics of the bubbles. A brief explanation of the foundations of the BEM in axi-symmetric domains was given in order to understand the essence of the method.

Experiments have been carried out with two different viscous liquids that have allowed to explore wide ranges of the Bond and capillary numbers keeping the effect of the inertia of the liquid small. Good qualitative agreement has been found between numerical and experimental results. The known scaling law for the volume of a bubble at detachment from the bottom of an unconfined liquid has been extended to take into account the presence of conical or cylindrical walls. For a conical reservoir, the semi-angle of the cone appears as an extra factor $\alpha^{-1/4}$ multiplying the standard $(Ca/Bo)^{3/4}$ scaling. For a cylindrical reservoir, the exponent may change from $3/4$ to 1 when the radius of the cylinder decreases.

The results of the work may have a bearing on the methods of enhanced oil recovery, where properly shape injection nozzles may allow optimizing the volume of the bubbles generated in oil production pipes without having to change the flow rate of gas or the foams injection in homogeneous or fractured reservoirs.

Acknowledgments Authors acknowledge the IPN for its partial support through projects SIP20131821 and SIP20131821-IPN, and also acknowledge the CONACyT for its partial support through the project SENER-CONACyT 146735.

Appendix A. The Green's Functions for Axisymmetric Flow

This Appendix lists Green functions for axisymmetric flow generated by a ring force of unit strength located at (x_0, r_0) and pointing in the direction \mathbf{e}_k with $k = r, x$. Defining the following quantities in cylindrical coordinates

$$\begin{aligned} Z &= x - x_0 \\ L &= \sqrt{Z^2 + (r + r_0)} \\ D &= \sqrt{Z^2 + \sqrt{Z^2 + (r + r_0)}} \\ S &= \sqrt{Z^2 + r^2 + r_0^2} \\ m &= \frac{2(r r_0)^{\frac{1}{2}}}{L} \end{aligned}$$

and elliptic integrals

$$\begin{aligned} K(m) &= \int_0^{\frac{\pi}{2}} \frac{d\theta}{\sqrt{1 - m^2 \sin^2 \theta}} \\ E(m) &= \int_0^{\frac{\pi}{2}} \sqrt{1 - m^2 \sin^2 \theta} d\theta, \end{aligned}$$

we have

$$\begin{aligned} G_x^x &= 4 \frac{r}{L} \left(K + E \frac{Z^2}{D^2} \right) \\ G_r^x &= 2 \frac{Z}{L} \left(K - E \frac{S^2 - r^2}{D^2} \right) \\ G_x^r &= 2 \frac{r Z}{r_0 L} \left(-K + E \frac{S^2 - 2r_0^2}{D^2} \right) \end{aligned}$$

$$\begin{aligned}
G_r^r &= 2 \frac{1}{r_0 L} \left[-k (S^2 + Z^2) - E \left(L^2 + \frac{Z^2 S^2}{D^2} \right) \right] \\
T_{xx}^x &= 8 \frac{r Z^3}{D^2} \left(K - E \frac{4 S^2}{D^2} \right) \\
T_{xx}^x &= T_{rx}^x = -4 \frac{Z^2}{D^2 L} \left[K \frac{S^2 - 2r^2}{L^2} - E \left(1 + \frac{8r_0^2 (2r_0^2 - s^2)}{D^2 L^2} \right) \right] \\
T_{rx}^x &= -4 \frac{r Z}{L} \left[K \left(\frac{1}{r^2} + \frac{2Z^2}{D^2 L^2} \right) - \frac{E}{D^2} \left(6 - S^2 \left(\frac{1}{r^2} + \frac{8Z^2}{D^2 L^2} \right) \right) \right] \\
T_{xx}^r &= -4 \frac{r Z}{r_0 D^2 L} \left[K \frac{2r_0^2 - S^2}{L^2} - E \left(1 + \frac{8r_0^2 (2r^2 - S^2)}{D^2 L^2} \right) \right] \\
T_{xx}^r &= T_{rx}^r = -4 \frac{Z}{r_0} \left[K \left(\frac{Z^2 S^2}{D^2 L^2} - 2 \right) + \frac{E}{D^2} \left(2S^2 - Z^2 - \frac{16r^2 r_0^2 Z^2}{D^2 L^2} \right) \right] \\
T_{rx}^r &= -4 \frac{r}{L} \left[\frac{K}{r_0} \left(\frac{Z^2 (S^2 - 2r_0^2)}{D^2 L^2} - \frac{r^2 - r_0^2 - 2Z^2}{r^2} \right) \right. \\
&\quad \left. + \frac{E}{D^2} \left(\frac{8r_0 Z^2 (S^2 - 2r^2)}{D^2 L^2} + \frac{r^2 (r^2 + r_0^2) - S^2 (r_0^2 + 2Z^2)}{r^2 r_0} \right) \right]
\end{aligned}$$

References

- Ajaev VS, Homsy GM (2006) Modeling shapes and dynamics of confined bubbles. *Ann Rev Fluid Mech* 38:277
- Bird RB, Armstrong RC, Hassager O (1987) Dynamics of polymeric liquids. Wiley, New York
- Cheng Alexander HD, Cheng Daisy T (2005) Heritage and early history of the boundary element method. *Eng Anal Boundary Element* 29:268–302
- Clift R, Grace JR, Weber ME (1978) Bubbles, drops, and particles. Academic Press, New York
- Corchero G, Medina A, Higuera FJ (2006) Effect of wetting conditions and flow rate on bubble formation at orifices submerged in water. *Colloids Surf A Physicochem Eng Aspects* 290:41
- Costabel Martin, (1986), Principles of boundary element methods. Technische Hochschule Darmstadt, lectures given at the first graduate summer course in computational physics “Finite Elements in Physics” Lausanne, pp 1–10
- Davidson JF, Schuler BG (1960) Bubble formation at an orifice in an inviscid liquid. *Trans Inst Chem Eng* 38:335–342
- Higuera FJ (2005) Injection and coalescence of bubbles in a very viscous liquid. *J Fluid Mech* 530:369
- Hirasaki GJ, Lawson JB (1985) Mechanisms of foam flow in porous media: apparent viscosity in smooth capillaries. *Sot Pet Eng J* 25(2):176–190
- Hirasaki GJ, Miller CA, Pope GA (2006) Surfactant based enhanced oil recovery and foam mobility control. In: 3rd annual and final technical report for DOE project (DE-FC26-03NT15406), February
- Kovscek AR, Tretheway DC, Persoff P, Radke CJ (1995) Foam flow through a transparent rough-walled rock fracture. *J Pet Sci Eng* 13:75–86

- Leighton TG, Fagan KJ, Field JE (1991) Acoustic and photographic studies of injected bubbles. *Eur J Phys* 12:77
- Longuet-Higgins M, Kerman BR, Lunde K (1991) The release of air bubbles from an underwater nozzle. *J Fluid Mech* 230:365–390
- López-Villa A, Medina A, Higuera FJ (2011) Bubble growth by injection of gas into viscous liquids in cylindrical and conical tubes. *Phys Fluids* 23:102102
- Manga M, Stone HA (1994) Interactions between bubbles in magmas and lavas: effects of the deformation. *J Volcanol Res* 63:269–281
- Marmur A, Rubin E (1976) A theoretical model for bubble formation at an orifice submerged in an inviscid liquid. *Chem Eng Sci* 31:453–463
- Oguz HN, Prosperetti A (1993) Dynamics of bubble growth and detachment from a needle. *J Fluid Mech* 257:111
- Oguz HN, Zeng J (1997) Axisymmetric and three-dimensional boundary integral simulations of bubble growth from an underwater orifice. *Eng Anal Boundary Element* 19:319
- Pozrikidis C (1992) Boundary integral and singularity methods for linearized viscous flows. Cambridge University Press, Cambridge
- Pozrikidis C (2002) A practical guide to boundary element methods. Chapman and Hall/CRC, New York
- Räbiger N, Vogelpohl A (1986) Bubble formation and its movement in Newtonian and non-newtonian liquids. In: Cheremisinoff NJ (ed) *Encyclopedia of fluid mechanics*, vol. 3, chap. 4. Gulf Publishing Company, Houston
- Ramakrishna S, Kumar R, Kuloor NR (1968) Studies in bubble formation—I: Bubble formation under constant flow conditions. *Chem Eng Sci* 24:731
- Russ JC (2002) *The image processing handbook*. CRC Press, Boca Raton
- Sadhal SS, Ayyaswamy PS, Chung JN (1997) *Transport phenomena with drops and bubbles*, chap. 7. Springer-Verlag, Berlin
- Sahagian DL (1985) Bubble migration and coalescence during solidification of basaltic lava flows. *J Geol* 93:205–211
- Tsuge H (1986) Hydrodynamics of bubble formation from submerged orifices. In: Cheremisinoff NP (ed) *Encyclopedia of fluid mechanics*, vol. 3. Gulf Publishing Company, Houston (chap. 9)
- Witherspoon PA, Radke CJ, Shikari Y, Pruess K, Persoff P, Benson SM, Wu YS (1987) Feasibility analysis and development of foam-protected underground natural gas storage facility. In: *Proceedings of the operating section, American Gas Association*, Paper #87-DT-110, pp 539–549
- Wong H, Rumschitzki D, Maldarelli C (1998) Theory and experiment on the low-Reynolds-number expansion and contraction of a bubble pinned at a submerged tube tip. *J Fluid Mech* 356:93
- Wraith AE, Kakutani T (1974) The pressure beneath a growing rising bubble. *Chem Eng Sci* 29:1
- Zhang L, Shoji M (2001) Aperiodic bubble formation from a submerged orifice. *Chem Eng Sci* 53:71

<http://www.springer.com/978-3-319-00115-9>

Experimental and Computational Fluid Mechanics

Klapp, J.; Medina Ovando, A. (Eds.)

2014, XXIV, 473 p. 293 illus., 164 illus. in color.,

Hardcover

ISBN: 978-3-319-00115-9